

Online Supplementary Information

Quasi-Anisotropic Benefits in Electrospun Nickel-Cobalt-Manganese Oxide Nano-Octahedron as Anode for Lithium-ion Batteries

JinKiong Ling,^{a,b} Chelladurai Karuppiah,^c Santanu Das^d, Vivek Kumar Singh^d, Izan Izwan Misnon,^{a,b} Mohd Hasbi Ab Rahim,^{a,b} Shengjie Peng^{e*}, Chun-Chen Yang,^{c,f,g*} and Rajan Jose^{a,b*}

^a*Center of Advanced Intelligent Materials, Universiti Malaysia Pahang, 26300 Kuantan, Pahang Darul Makmur, Malaysia.*

^b*Faculty of Industrial Sciences & Technology, University Malaysia Pahang, Pahang Darul Makmur, Malaysia*

^c*Battery Research Center for Green Energy, Ming Chi University of Technology, New Taipei City, 24301, Taiwan, R.O.C.*

^d*Department of Ceramic Engineering, Indian Institute of Technology (Banaras Hindu University), Varanasi, 221005, Uttar Pradesh, India.*

^e*Jiangsu Key Laboratory of Electrochemical Energy Storage Technologies, College of Material Science and Technology, Nanjing University of Aeronautics and Astronautics, Nanjing 210016, PR China.*

^f*Department of Chemical Engineering, Ming Chi University of Technology, New Taipei City, 24301, Taiwan, R.O.C.*

^g*Department of Chemical and Materials Engineering, Chang Gung University, Kwei-shan, Taoyuan 333, Taiwan, R.O.C.*

*Corresponding Authors:

(Shengjie Peng) pengshengjie@nuaa.edu.cn; (Chun-Chen Yang) ccyang@mail.mcut.edu.tw; (Rajan Jose) rjose@ump.edu.my

Supplementary Information S1: Repeatability of Octahedron through Electrospinning

In order to validate the formation of nano-octahedron via electrospinning techniques, similar procedure was repeated under similar conditions and pilot scale multi-needle electrospinning instrument to synthesis the nano-octahedron. The FESEM images for the second and third trials were shown in **Figure S1**, where formation of nano-octahedron can be observed during both second and third trials, validating the repeatability of the formation mechanism. During the fourth trial, the electrospinning procedure was carried out under uncontrolled/ambient atmosphere, where both the temperature and humidity fluctuated around

~25°C and 60%, respectively. Under such conditions, rapid melting of the electrospun mat and formation of irregular particle after annealing was observed. Both lower temperature and higher humidity leads to slower solvent evaporation rate, leading to the melting of electrospun mat on the collector, leading to the formation of irregular particle after annealing. This additional experimental work highlighted the vitality of controlled environment (both temperature ~30°C and humidity ~40%) in the production of nano-octahedron via electrospinning techniques.

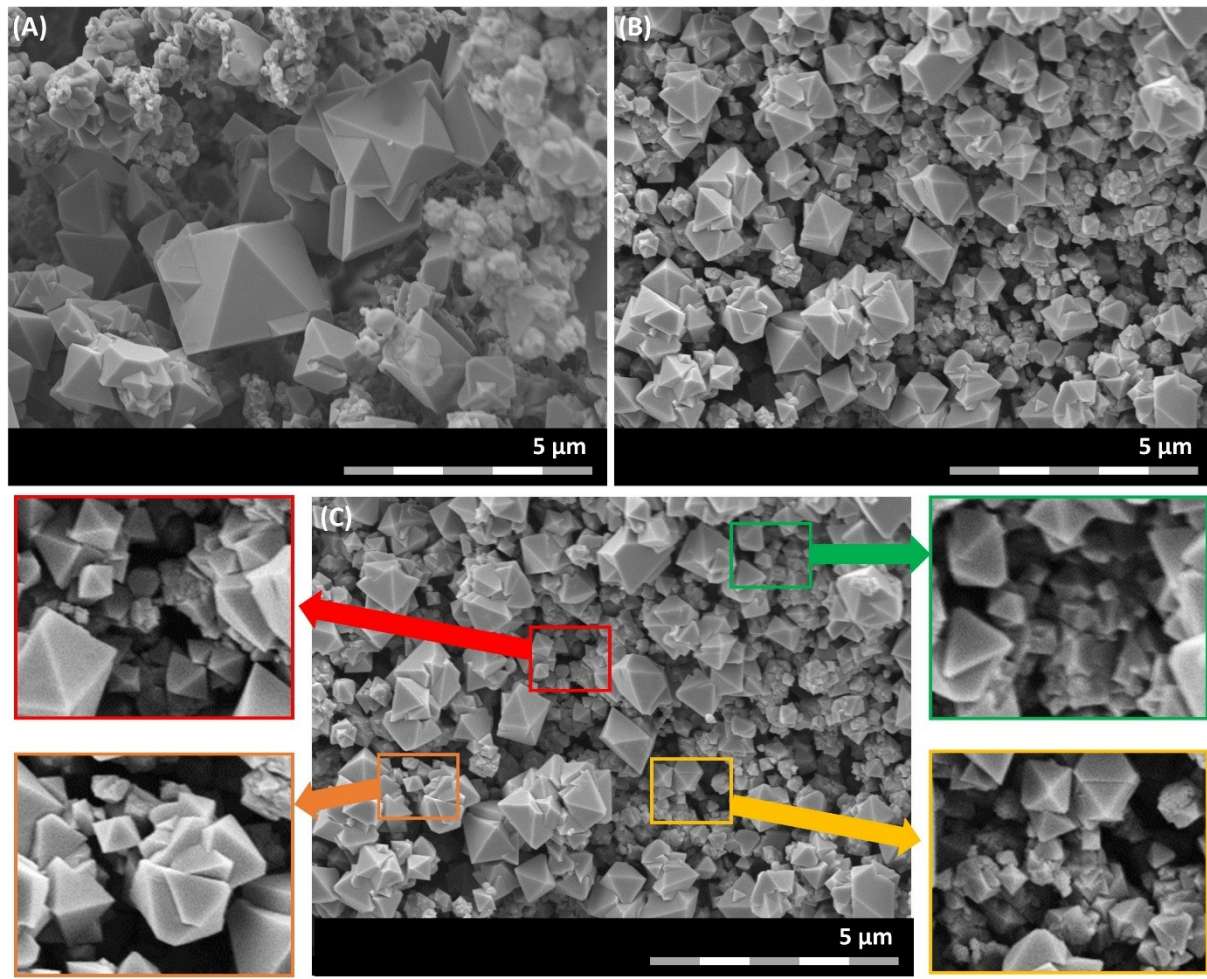


Figure S1. Repeatability in production of octahedron. FESEM observation confirmed that the octahedron was formed during both the second (a) and third (b) trials, validating the repeatability of octahedron production using pilot-scale multi-needles electrospinning instrument under controlled environment. (c) Magnified images for 4 area, showing medium size octahedron particles at ~300-400 nm and irregular-shaped particles at size <150 nm.

Supplementary Information S2: Particle size

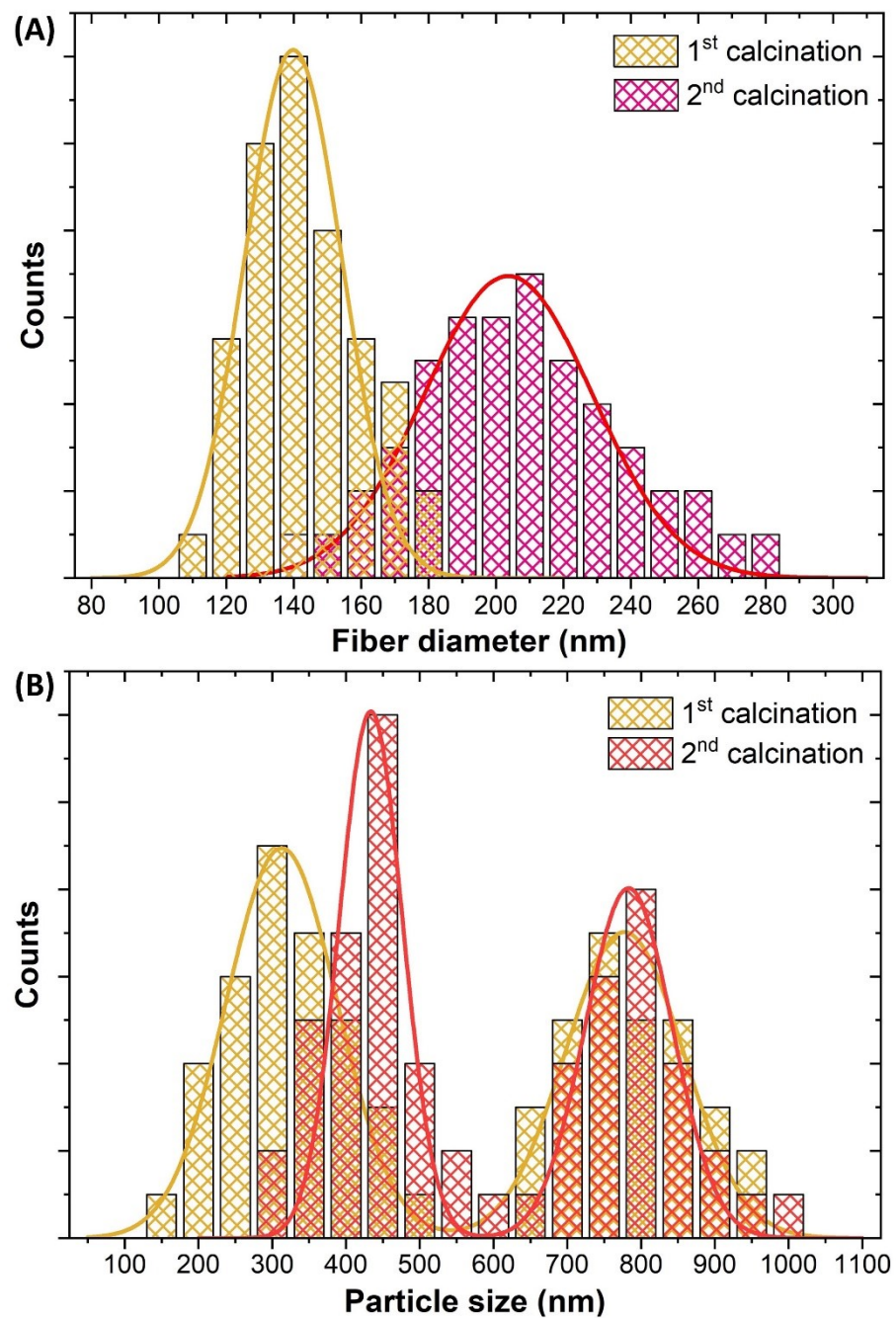


Figure S2. Size distribution of fiber and octahedron. The size distribution histogram for (a) fiber and (b) octahedron both after 1st calcination at 600°C for 3 hours and 2nd calcination at 850°C for 6 hours.

Supplementary Information S3: High resolution transmission electron microscope (HRTEM)

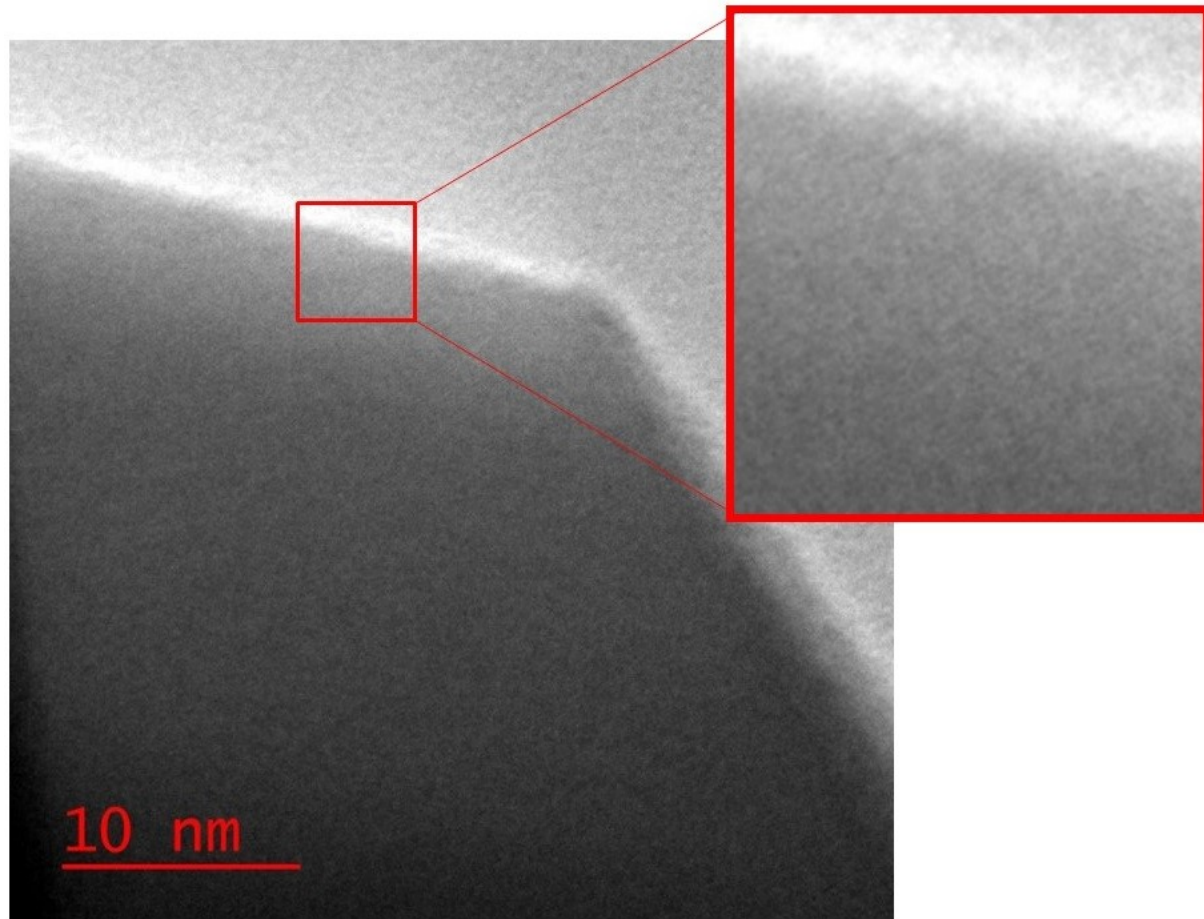


Figure S3. HRTEM image for no-NCM. Fuzzy lattice fringes can be observed at the edge of the sample where either the thickness is smaller or the particles are less densely arranged. The appearance of fuzzy lattice confirmed the speculation of densely arranged particles and rules out the existence of amorphous phase.

Supplementary Information S4: Crystal structure (XRD)

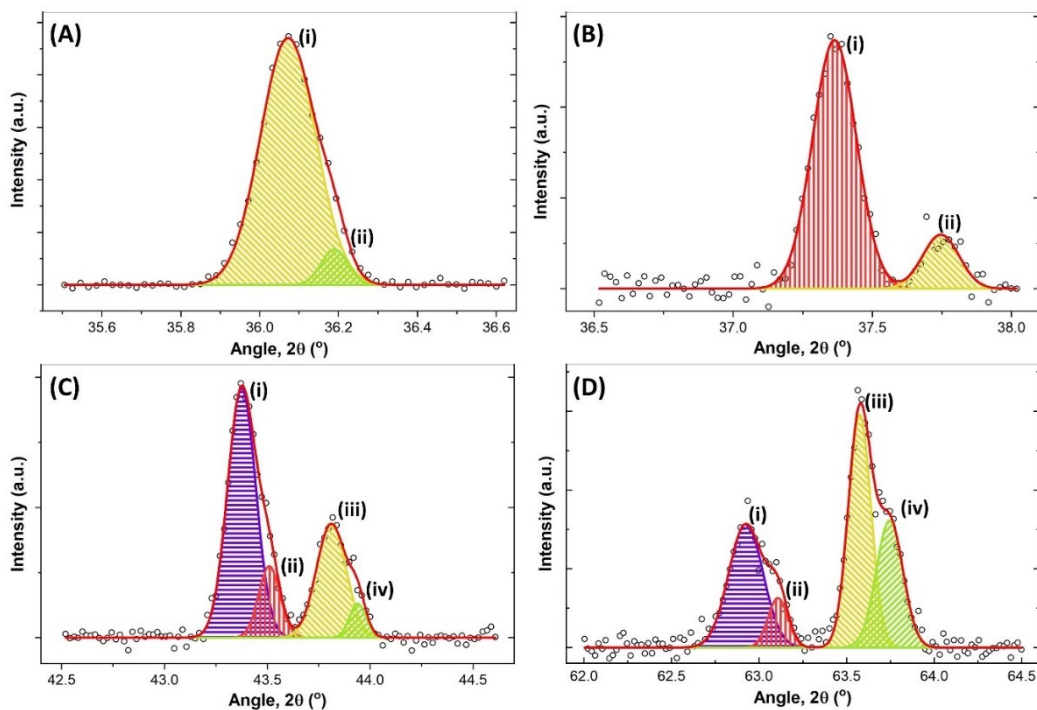


Figure S4.1. Deconvoluted XRD peaks for nf-NCM. Four major intense peaks from XRD spectrum of nf-NCM were deconvoluted, (A) 36° , (B) 37° , (C) 43° , and (D) 63° . The crystal phase related to each deconvoluted peaks was designated in Table S3.

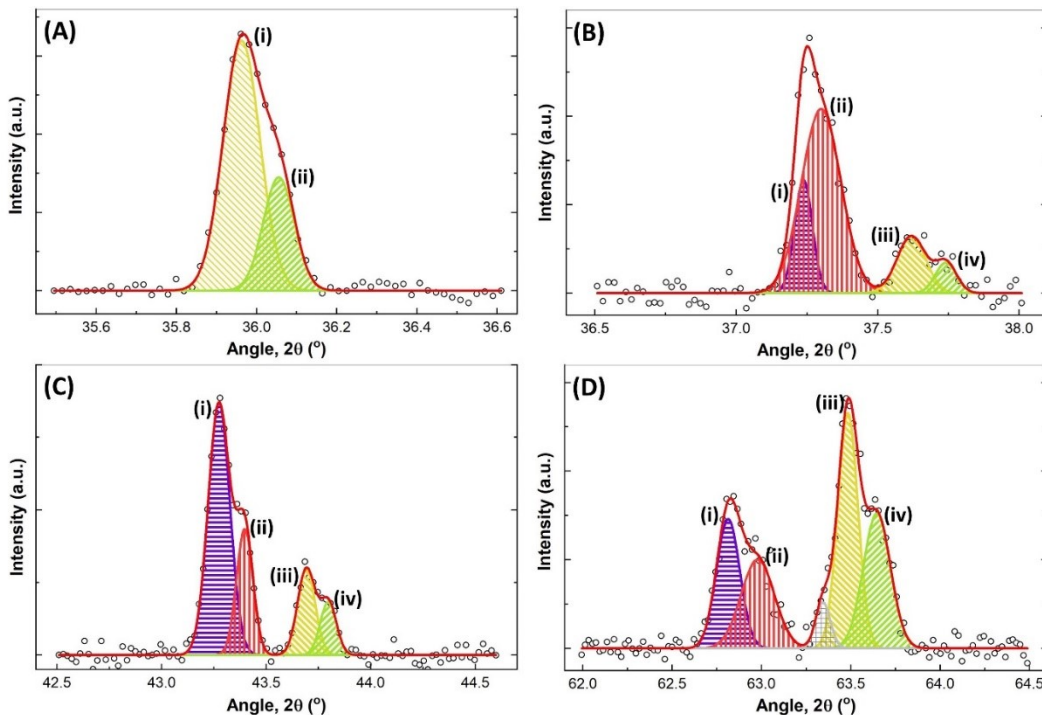


Figure S4.2. Deconvoluted XRD peaks for no-NCM. Four major intense peaks from XRD spectrum of nf-NCM were deconvoluted, (A) 36° , (B) 37° , (C) 43° , and (D) 63° . The crystal phase related to each deconvoluted peaks was designated in Table S3.

Table S1. Multiple phases from XRD analysis. Deconvoluted peaks for peak i, ii, iii, and iv in Figure S3.1-2. The phases associated with respective peaks were assigned, together with the oxidation state of the corresponding element.

Peak		nf-NCM				no-NCM			
		Center	FWHM	Phase	OS	Center	FWHM	Phase	OS
36°	600°C	36.09°	0.354	Co ₂ MnO ₄	Co ²⁺	35.96°	0.333	Co ₂ MnO ₄	Co ²⁺
36°	i	36.07°	0.165	Co ₂ MnO ₄	Co ²⁺	35.96°	0.109	Co ₂ MnO ₄	Co ²⁺
	ii	36.19°	0.080	Co ₂ MnO _{4.5}	Co ³⁺	36.06°	0.092	Co ₂ MnO _{4.5}	Co ³⁺
37°	i	37.36°	0.185	NiO/Ni ₆ MnO ₈	Ni ²⁺	37.24°	0.074	NiO/Ni ₆ MnO ₈	Ni ²⁺
	ii	37.75°	0.155	Co ₂ MnO ₄	Co ²⁺	37.30°	0.164	Ni ₃ O ₄ /Ni ₂ MnO _{4.5}	Ni ³⁺
	iii	-	-	-	-	37.62°	0.119	Co ₂ MnO ₄	Co ²⁺
	iv	-	-	-	-	37.74°	0.089	Co ₂ MnO _{4.5}	Co ³⁺
43°	i	43.37°	0.161	NiO/Ni ₆ MnO ₈	Ni ²⁺	43.27°	0.123	NiO/Ni ₆ MnO ₈	Ni ²⁺
	ii	43.51°	0.122	Ni ₃ O ₄ /Ni ₂ MnO _{4.5}	Ni ³⁺	43.40°	0.093	Ni ₃ O ₄ /Ni ₂ MnO _{4.5}	Ni ³⁺
	iii	43.81°	0.170	Co ₂ MnO ₄	Co ²⁺	43.69°	0.099	Co ₂ MnO ₄	Co ²⁺
	iv	43.94°	0.094	Co ₂ MnO _{4.5}	Co ³⁺	43.80°	0.091	Co ₂ MnO _{4.5}	Co ³⁺
63°	i	62.92°	0.231	NiO/Ni ₆ MnO ₈	Ni ²⁺	62.81°	0.153	NiO/Ni ₆ MnO ₈	Ni ²⁺
	ii	63.11°	0.133	Ni ₃ O ₄ /Ni ₂ MnO _{4.5}	Ni ³⁺	62.98°	0.219	Ni ₃ O ₄ /Ni ₂ MnO _{4.5}	Ni ³⁺
	iii	63.57°	0.152	Co ₂ MnO ₄	Co ²⁺	63.48°	0.133	Co ₂ MnO ₄	Co ²⁺
	iv	63.74°	0.180	Co ₂ MnO _{4.5}	Co ³⁺	63.65°	0.180	Co ₂ MnO _{4.5}	Co ³⁺

Supplementary Information S5: Element distribution (HRTEM-EDS)

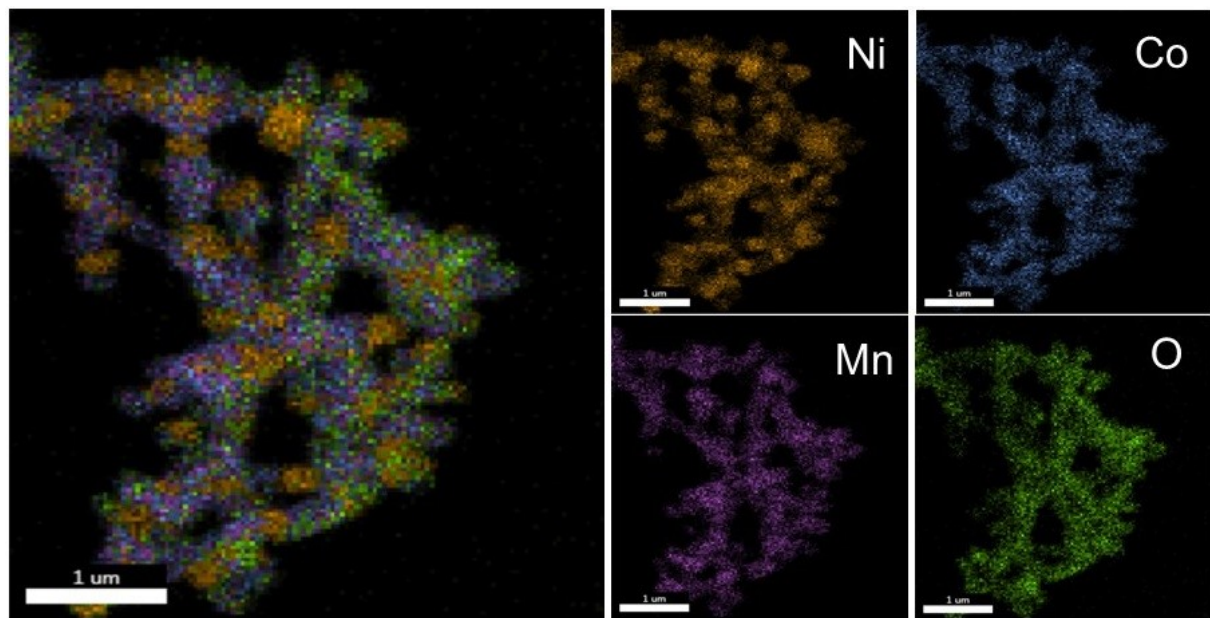


Figure S5.1. Elemental distribution of nf-NCM. All the elements are distributed throughout the samples, with region of higher nickel content, region of Ni-Mn mixture, as well as region of Co-Mn mixture can be observed. These regions match the co-existence of NiO, Ni₆MnO₈, and Co₂MnO₄ crystal phases observed in XRD spectra.

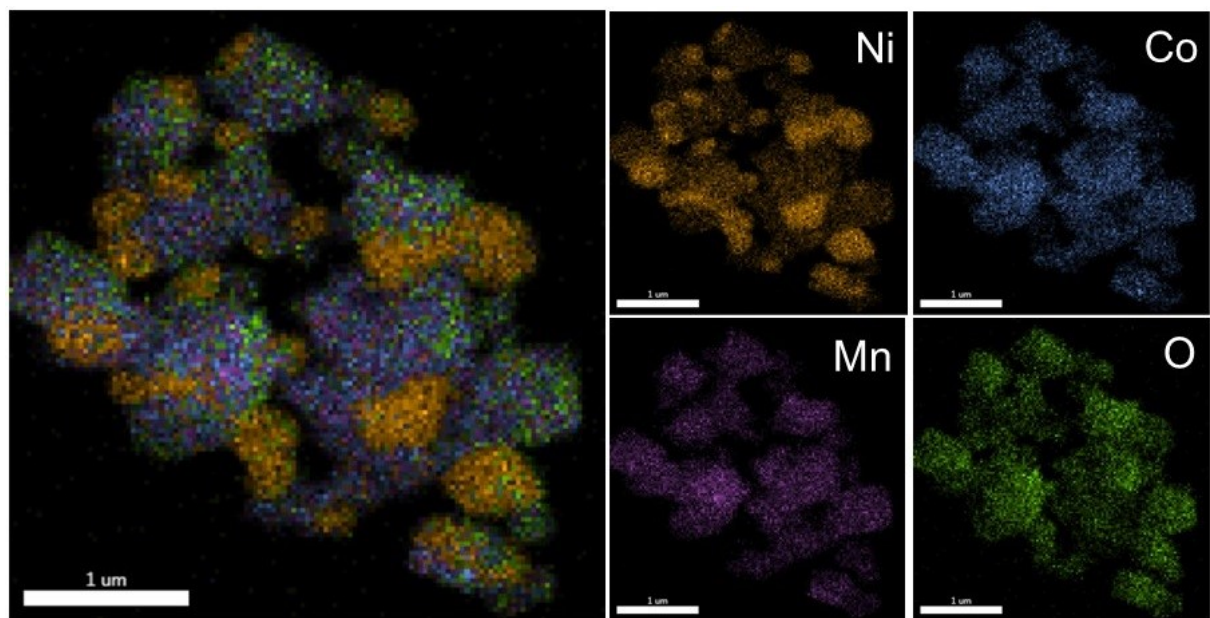


Figure S5.2. Elemental distribution of no-NCM. All the elements are distributed throughout the samples, with region of higher nickel content, region of Ni-Mn mixture, as well as region of Co-Mn mixture can be observed. These regions match the coexistence of NiO, Ni₆MnO₈, and Co₂MnO₄ crystal phases observed in XRD spectra.

Supplementary Information S6: Surface chemistry

Table S2. Designated XPS peaks for both nf-NCM and no-NCM. The binding energy, full-width at half maximum, intensity, as well as respective attributor to the deconvoluted peaks for both nf-NCM and no-NCM samples.

Peaks	nf-NCM				no-NCM			
	BE (eV)	FWHM	Intensity (a.u.)	Attributor	BE (eV)	FWHM	Intensity (a.u.)	Attributor
Ni 2p3	853.51	1.191	2903.24	Ni ²⁺	853.57	1.324	1427.98	Ni ²⁺
	854.77	3.240	3615.36	Ni ³⁺	854.67	3.131	1760.03	Ni ³⁺
	860.44	3.963	2007.68	Sat.	860.28	2.966	930.04	Sat.
	864.34	2.668	258.57	Sat.	863.01	2.139	168.95	Sat.
Ni 2p1	871.01	1.489	1225.07	Ni ²⁺	870.68	1.075	496.01	Ni ²⁺
	872.37	2.437	1322.56	Ni ³⁺	871.87	1.808	812.43	Ni ³⁺
	876.53	5.140	457.84	Sat.	873.41	2.672	251.62	Sat.
	877.58	4.015	783.33	Sat.	878.83	4.517	445.89	Sat.
Co 2p3	779.53	2.976	2514.06	Co ²⁺	779.45	2.328	2651.69	Co ²⁺
	782.22	2.319	560.95	Co ³⁺	781.60	1.977	478.63	Co ³⁺
	785.37	6.013	818.02	Sat.	784.02	8.005	685.67	Sat.
Co 2p1	794.78	2.254	867.57	Co ²⁺	794.57	1.910	1002.08	Co ²⁺
	796.68	2.683	444.76	Co ³⁺	796.47	2.426	484.06	Co ³⁺
	801.75	5.299	388.67	Sat.	802.05	5.769	345.66	Sat.
Mn 2p3	636.83	2.307	1963.17	Mn ³⁺	636.97	2.121	1392.00	Mn ³⁺
	640.74	3.502	2363.38	Mn ⁴⁺	641.03	3.947	2213.45	Mn ⁴⁺
	643.38	7.335	1409.88	Sat.	644.02	6.408	415.35	Sat.
Mn 2p1	652.87	3.162	1803.91	Mn ⁴⁺	652.83	2.788	1393.70	Mn ⁴⁺
	655.49	2.364	204.25	Sat.	654.72	2.355	347.24	Sat.
O 1s	528.95	0.989	10672.97	M-O	528.98	1.195	9713.75	M-O
	529.95	3.092	2646.37	M-OH	530.32	1.200	2326.65	M-OH

Supplementary Information S7: Lithium Storage Performance Comparison

Table S3. Lithium storage performance comparison. A comparison between the reported data and results reported on previous study on nanostructure transition metal oxide anode, especially nickel-, cobalt-, and manganese- based analogues.

Materials	Morphology	Methods	Gravimetric specific capacity at 100 mA g ⁻¹ (mAh g ⁻¹)	Cycling stability (mAh g ⁻¹ /cycle/mA g ⁻¹)	ref
Co ₃ O ₄	Particles	Template	750.2	549/40/100	1
Co ₃ O ₄ /CoO	Bulk	Freeze-drying	939.0	990/50/100	2
NiO	Urchin	Hydrothermal	1027.0	909/50/100	3
NiO	Hollow fiber	Electrospinning	1174.0	956/400/200	4
NiO	Bulk	Hydrothermal	529.0	413/100/100	5
MnO ₂	Wire	Template	1160.0	708/50/100	6
MnO ₂ /rGO	Rod	Grinding	397	200/200/100	7
NiCo ₂ O ₄	Wire	Hydrothermal	1048.8	763/50/500	8
NiCo ₂ O ₄	Wire	Hydrothermal	1520.0	413/50/100	9
NiCo ₂ O ₄	Sheet	Microwave	891.0	767/50/100	10
NiCo ₂ O ₄	Dried plum-like	Spray pyrolysis	855.0	801/50/100	11
MnCo ₂ O ₄ /NiCo ₂ O ₄	Rod	Hydrothermal	968.0	330/100/100	12
MnCo ₂ O ₄ /NiCo ₂ O ₄ /NiMn ₂ O ₄	Hexagonal	Template	780.0	>400/100/150	13
Co ₂ MnO ₄ /NiO/Ni ₆ MnO ₈	Fiber	Electrospinning	1074.8	291/500/1000	This work
Co ₂ MnO ₄ /NiO/Ni ₆ MnO ₈	Octahedron	Electrospinning	1183.5	71/500/1000	This work

References

1. X. Leng, S. Wei, Z. Jiang, J. Lian, G. Wang and Q. Jiang, *Scientific Reports*, 2015, **5**, 16629.
2. H. Park, K. Kim, K. Jeong, J. S. Kang, H.-H. Cho, B. Thirumalraj, Y.-E. Sung, H. N. Han, J.-H. Kim, D. C. Dunand and H. Choe, *Applied Surface Science*, 2020, **525**, 146592.
3. A. K. Mondal, D. Su, Y. Wang, S. Chen, Q. Liu and G. Wang, *Journal of Alloys and Compounds*, 2014, **582**, 522-527.
4. J. H. Oh, M. Su Jo, S. M. Jeong, C. Cho, Y. C. Kang and J. S. Cho, *Journal of Industrial and Engineering Chemistry*, 2019, **77**, 76-82.
5. M. G. Ortiz, A. Visintin and S. G. Real, *Journal of Electroanalytical Chemistry*, 2021, **883**, 114875.
6. M.-S. Wu and P.-C. J. Chiang, *Electrochemistry Communications*, 2006, **8**, 383-388.
7. Y. Meng, Y. Liu, J. He, X. Sun, A. Palmieri, Y. Gu, X. Zheng, Y. Dang, X. Huang, W. Mustain and S. L. Suib, *ACS Applied Energy Materials*, 2021, **4**, 5424-5433.

8. X. Zhou, G. Chen, J. Tang, Y. Ren and J. Yang, *Journal of Power Sources*, 2015, **299**, 97-103.
9. G. Chen, J. Yang, J. Tang and X. Zhou, *RSC Advances*, 2015, **5**, 23067-23072.
10. A. K. Mondal, D. Su, S. Chen, K. Kretschmer, X. Xie, H.-J. Ahn and G. Wang, *ChemPhysChem*, 2015, **16**, 169-175.
11. T. Li, X. Li, Z. Wang, H. Guo and Y. Li, *Journal of Materials Chemistry A*, 2015, **3**, 11970-11975.
12. R. Solmaz, B. D. Karahan and O. Keles, *Journal of Applied Electrochemistry*, 2020, **50**, 1079-1089.
13. D. McNulty, H. Geaney and C. O'Dwyer, *Scientific Reports*, 2017, **7**, 42263.